Small Morphology Variations Effects on Plasmonic Nanoparticle Dimer Hotspots†

Yu Huang,[*a] Yun Chen,[a] Ling-Ling Wang,[a] and Emilie Ringe[*bc]

[a]*School of Physics and Electronics, Hunan University, Changsha 410082, China*

[b]*Department of Materials Sciences and Metallurgy, University of Cambridge, 27 Charles Babbage Road, Cambridge CB3 0FS, UK*

[c]*Department of Earth Sciences, University of Cambridge, Downing Street, Cambridge CB2 3EK, UK*

[*]*E-mail: huangyu@hnu.edu.cn, er407@cam.ac.uk*

† Electronic supplementary information (ESI) available. See DOI:

TOC

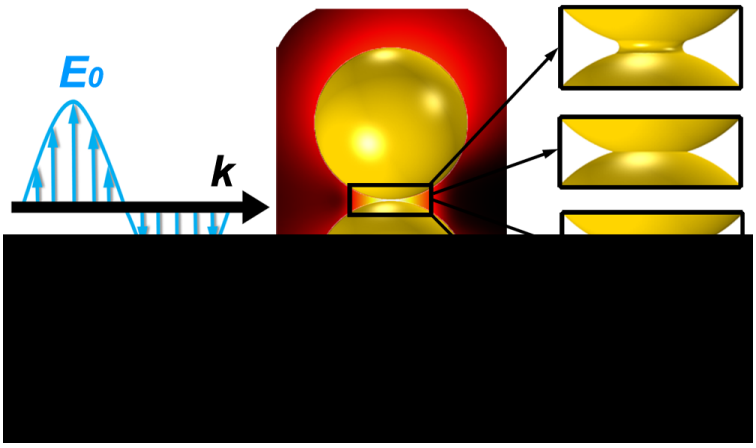

Beyond the ideal nanosphere dimer hotspot model, small morphology variations can have great influences on the plasmonic properties.

Abstract

Plasmonic nanoparticle (NP) dimer structures, forming highly intense areas of field enhancement called hotspots, have been the focus of extensive investigations due to their phenomenal light manipulating abilities. However, the actual morphology of the NP hotspot is usually distinct from the ideal nanosphere dimer model. In this study, we demonstrate numerically that small morphology variations in the presence of nanobridge, nanocrevice, nanofacet or nanoroughness, can have a major impact on the plasmonic properties of the whole system. The resonance wavelength and magnitude of the near-field enhancement are found to acutely depend on the interparticle gap geometry. The hotspot may become degenerated or regenerated. We also observe that the hybridized modes excited under longitudinal polarizations, including the bonding dipole plasmon (BDP) and charge charge transfer plasmon (CTP) modes, can be assigned to the bonding longitudinal antenna plasmon (LAP) modes for all gap geometries. These results provide means to understand and justify the ongoing poor reproducibility of surface enhanced Raman scattering (SERS) substrates, stressing the importance of precision plasmonics.

Keywords: hotspot, SERS, nanoparticle dimer, near-field enhancement, precision plasmonics, gold nanoparticles

Introduction

Owing to high sensitivity, fast response and fingerprint identification, surface enhanced Raman scattering (SERS) is now an established, powerful analytical tools for chemical and biological sensing.[1-3] The electromagnetic (EM) enhancement mechanism, a dominant contribution to SERS enhancement,[2,4] involves extreme light confinement and huge local electric field amplification resulting from localized surface plasmon resonances (LSPRs) sustained on plasmonic nanostructures.[5] The enhancement factor (EF) of SERS is approximately proportional to the fourth power of the local electric field intensity.[2,4,6,7] EFs can reach ~10^8 in a hotspot, enabling single molecule SERS.[8-10] However the reproducibility is often a challenge.[1,2,11,12] Enhancement and hotspots are of importance beyond SERS, for instance in surface enhanced infrared absorption (SEIRA),[2,13] nonlinear optics,[14-16] nano-optoelectronics,[17,18] and quantum plasmonics,[19,20] to name a few.

An EM hotspot with significant field enhancement is typically formed in the nanosized gap separating two plasmonic nanoparticles (NPs). Since they are easily fabricated and modeled, plasmonic dimers have been extensively studied both experimentally and theoretically.[2,4,21-26] In dimers, for instance, the dipolar LSPRs of individual NPs hybridize to form the bonding dipole plasmon (BDP) mode, giving rise to large local electric fields enhancements.[23,27] This field enhancement, as well as all other LSPR properties, i.e., energy, width, and near-field distributions, strongly depends on the NP's size, shape, orientation, composition, and the surrounding dielectric environment.[3,5,28] It is thus unsurprising that small variations in the gap

morphology such as corner rounding,[29,30] the presence of facets,[31] facet alignment,[25] and NP-on mirror geometry[32,33] can dramatically modify the near- and far-field plasmonic properties of the system.

The morphology changes are expected owing to the tendency of NPs to form faceted crystals rather than perfect sphere,[33-35] as well as a multitude of potential post-synthesis modifications such as meting and fusing under intense illumination.[36-39] Together, these effects lead to a complex set of possible gap geometries, including nanobridge,[40-43] nanocrevice,[4,44-46] nanofacet,[25,33,47,48], nanoroughness[21,24,49-52] for instance and even the combination of several featured morphologies.

Here, we present a systematic numerical study of the effects of these local morphology changes on the plasmonic properties of dimer hotspots. We explore their effects on the plasmon resonance, light localization and spectral distribution. Our results can contribute to explaining many discrepancies and inconsistencies encountered in SERS experiments, stressing the importance of precisely fabricating and characterizing plasmonic systems, i.e., precision plasmonics.[24,53,54]

Methods

As a blank control, the computational model for a typical, idealized hotspot is composed of two R = 50 nm Au nanospheres separated by a 1 nm gap which is shown in Fig. 1(a). Such narrow gap gives rise to highly enhanced local electric fields while ensuring that quantum

effects remain weak and classical electrodynamics, adequate.[55,56] R = 50 nm is the optimal size for Au NP dimers to achieve maximum near-field enhancement.[26] Full electrodynamic calculations are performed using finite element method (FEM) based on COMSOL Multiphysics. The hotspot systems are illuminated by a plane wave with a polarization along the dimer axis. The surrounding media is vacuum (n = 1). The dielectric function of Au is modeled by the Lorentz-Drude dispersion model fitting the experimental data in Palik:[57,58]

$$\varepsilon(w) = 1 - \frac{f_0 {w_p}^2}{w(w - i\Gamma_0)} + \sum_{j=1}^{m} \frac{f_j {w_p}^2}{({w_j}^2 - w^2) + iw\Gamma_j}, \qquad (1)$$

where the last term is the result of the Lorentz modification, w_p is the plasma frequency with oscillator strength f_0 and damping constant Γ_0, m is the number of oscillators with frequency w_j, strength f_j and damping constant Γ_j. The fitting parameter values are f_0 = 0.760, w_p = 9.03 eV, Γ_0 = 0.053 eV, f_1 = 0.024, Γ_1 = 0.241 eV, w_1 = 0.415 eV, f_2 = 0.010, Γ_2 = 0.345 eV, w_2 = 0.830 eV, f_3 = 0.071, Γ_3 = 0.870 eV, w_3 = 2.969 eV, f_4 = 0.601, Γ_4 = 2.494 eV, w_4 = 4.304 eV, f_5 = 4.384, Γ_5 = 2.214 eV, w_5 = 13.32 eV.[58]

For near-field spectral characteristics, an average near-field enhancement approach is used. We take the spatial average of EF = $|\boldsymbol{E}|^4/|\boldsymbol{E}_0|^4$ as follows:[56,59]

$$\langle EF \rangle = \frac{\iint (|\boldsymbol{E}|^4/|\boldsymbol{E}_o|^4)\, dS}{S} \qquad (2)$$

where $|\boldsymbol{E_0}|$ = 1 V/m is the amplitude of incident field, $\boldsymbol{E}$ is the local electric field, S is a 1-nm-thick cross section above the NP surface in the symmetry plane, as indicated by grey outlines in Fig. 1(a). The grey area approximates a monolayer of analyte molecules physically adsorbed onto the surface. And SERS can be explained as a “twofold” EM enhancement

process: the EM fields of the incident photons are first enhanced at the vicinity of hotspots, and then the re-emitted Stokes Raman scattering photons are enhanced again by surface plasmons. Thus the physical significance of <EF> can be understood as the averaged SERS EF, assuming the Stokes Raman shift approaches to zero and the coupling between the molecule and surface plasmons is negligible.[2,4,6,7,60] To ensure high accuracy of the numerical results, the minimum size of the adaptive meshing grid was set to be 0.2 nm around the gaps.

Results and discussion

To understand the effects of local hotspot geometry on plasmonic properties of Au dimers, we explored four different geometries that are described in the next sections: nanobridge, nanocrevice, nanofacet and nanoroughness. For each, we performed a systematic numerical calculations using COSMOL. In addition to COSMOL's standard output of wavelength-dependent electric field distribution (near-field), we used a recently developed approach to evaluate the surface charge density ρ and confirm the plasmonic nature of the modes:[59,61-63]

$$\rho = \frac{\varepsilon_0(n_x \cdot E_x + n_y \cdot E_y + n_z \cdot E_z)}{\delta(1-e^{-R/\delta})} \propto \left(n_x \cdot E_x + n_y \cdot E_y + n_z \cdot E_z\right), \qquad (3)$$

where ε_0 is the permittivity of vacuum, $\boldsymbol{n} = (n_x, n_y, n_z)$ is the outward normal vector of the NP surface, δ is the skin depth, the local electric field $\boldsymbol{E} = (E_x, E_y, E_z)$. This mapping approach help us determine the symmetry of the plasmon modes and recognize complicated and hybridized modes, as shown below.[59,62,63]

Most of the modes obtained for dimers can be understood in an analogous fashion to the modes commonly encountered in nanorods. The LSPRs in both comprise longitudinal antenna plasmon (LAP) modes with bonding characteristics, whose order can be described by *l* parameter.[31,64] *l* plus one equals the number of the surface charge poles (or antinodes). For example, a dipole mode possesses two poles, so $l = 1$. We have chosen to represent these various modes with symbols through the manuscript, as follows: the charge transfer plasmon (CTP) mode, $l = 0$, is marked as squares, the BDP mode, $l = 1$ (circles), the next higher bonding LAP mode, $l = 2$ (triangles), and finally we represent $l = 3$ with hexagons.

Nanobridge

We first consider the influence of nanobridges, i.e. a gap where the two NPs are connected by a conductive junction (Fig. 1). Owing to the intrinsic surface diffusion of atoms, SERS nanostructures may suffer morphological instability leading to bridge formation, even near room temperature.[65,66] Such bridges could also be deliberately formed, through direct fabrication of metallic bridges, introduction of conductive molecular linkers, or thermal coarsening.[40-43] In this geometry, charge can flow between the NPs, giving rise to the CTP mode that affects the dimer's optical properties.[42] We modelled this bridge as a thin Au junction in the shape of a truncated cylinder with radius *b* ranging from 2 to 15 nm connecting two spheres of 50 nm radius. To provide a better match to experimental

geometries, the junction was further smoothed by an arc tangent to the two particles, as shown in Fig. 1(a).

The calculated near-field wavelength-dependent <EF> spectra are plotted in Fig. 1(b). The peaks indicated by circle symbols are identified to be the BDP mode, also illustrated in Fig. 2. The broad, intense near-field enhancement of the Au dimer in the visible regime is mainly attributed to the BDP mode. Compared with the idealized, non-bridged dimer, the presence of the bridges dramatically decreases the field enhancement and slightly shifts the resonances to the blue region. As the bridge width 2*b* increases to 30 nm, the peak <EF> intensity decrease nearly exponentially, from 7.1×10^8 to 8.0×10^3, resulting into a rapid degeneration of hotspots, which is consistent with previous observations.[67] The results presented here highlight the significance of thermal stability in maintaining high EF enhancement in, e.g., SERS substrates.

Interestingly, another resonance is present at longer wavelengths for the bridged dimer, whose origin can be understood through near-field mapping of the plasmon modes. The top panels of Fig. 2 illustrate local electric field distributions (in the form of logarithmic $|\boldsymbol{E}|^4/|\boldsymbol{E}_0|^4$) and corresponding 3D surface charge distributions for the ideal Au nanosphere dimer at resonance wavelengths λ = 695, 570 nm. The maximum EF is 7.9×10^{10} and 5.0×10^9, respectively. Fig. 2(b) shows clearly the surface charge diagram "+ - — + -" ("—" means bonding) and reveals the BDP mode (resonance order l = 1,), while the latter in Fig. 2(d) demonstrates a higher-order bonding mode (l = 2, "+ - + — - + -"). There are clearly

three poles for each individual nanospheres, and the pole near the gap is deformed and reduced in size due to strong near-field coupling. The plasmon mapping for bridged dimers *b* =5 and 15 nm is shown in Fig. 2(i) and 2(k). Upon increasing the diameter of the conductive bridge, the BDP mode blueshifts to λ = 630, 575 nm, respectively, and enhanced local electric fields distribute more broadly around the bridges. The maximum EF decreases to 3.0×10^8 and 2.3×10^5 [Fig. 2(e) and 2(g)] for *b* =5 and 15 nm, respectively. This can be attributed to a weaker surface charge localization induced by charge flow through the bridge. The field enhancement sustained by the bonding *l* = 2 mode occurring at a shorter wavelength, e.g. λ = 550 nm for *b* = 5 nm, decreases to a maximum EF of 4.3×10^7 [Fig. 2(f)]. The increase in bridge width also gives rise to a prominent CTP mode, at λ = 1065 nm for *b* =15 nm [Fig. 2(l)]. This CTP mode, sometimes understood as the fundamental dipole mode or the bonding of monopole modes (*l* = 0, "+ — -"),[68] can sustain a large near-field enhancement with the maximum EF = 8.5×10^6 [Fig. 2(h)]. The trend in Fig. 1(b) indicates that a narrow bridge is expected to produce a CTP mode at longer wavelengths with even higher field enhancement, which can provide a design approach to plasmonic devices at infrared wavelengths.[42]

Nanocrevice

Another typical morphology feature for connected NPs is the nanocrevice due to coalescing during fabrication or post processing.[4,44-46] Here, we tailored the geometry of the crevice through the parameter *c*, which represents the intersecting face radius [Fig. 3(a)].

Fig. 3(b) shows the calculated <EF> spectra by increasing *c* from 5 (very sharp crevice) to 15 nm (broad crevice). Both the spectral line shapes and shifts are similar to those in Fig. 1(b) for bridged dimers. As *c* increases, the peak <EF> intensity of the BDP mode decreases and the resonance is blue shifted. A rising CTP mode can also be observed at longer wavelengths and the resonance, with a lower peak <EF> intensity, seems to be blue shifted as well. These effects are attributable to charge flow between the NPs enabled by the crevice geometry, akin the bridged dimers discussed above. One difference in <EF> trends is notable, however: instead of a constant decrease in <EF> with the bridge size, a significant jump of <EF> over the idealized dimer in the case of crevice is observed for c = 5 nm. Indeed, the peak <EF> intensity of the BDP mode at λ = 735 nm is 2.1×10^{10}, i.e. about 30 times larger than that of the idealized dimer.

Fig. 4(a) shows the corresponding local field distributions where the maximum EF reaches 5.0×10^{14} at the crevice. For the higher-order mode at λ = 640 nm, the maximum EF is 6.3×10^{13} [Fig. 4(b)]. An oblique view for the surface charge poles [Fig. 4(f)] shows that this higher-order mode is the bonding l = 2 mode. For c = 15 nm, the surface charge mapping in Fig. 4(g) and 4(f) clearly reveals the BDP and CTP modes. Even in this relatively obtuse crevice, the maximum EF can be as high as 2.0×10^{10} and 1.3×10^{10} for the BDP and CTP modes, respectively [Fig. 4(c) and 4(d)]. Such high maximum EFs are comparable with that of the idealized dimer, even though their averaged EFs in terms of <EF> (2.3×10^{6}, 5.8×10^{6}) are nearly two orders of magnitude lower. Therefore, the sharp feature induced by the

crevices may expand the upper limit of the near-field enhancement sustained by dimer gap hotspots, which is beneficial to single molecule detection.

Nanofacet

Plasmonic NPs are commonly faceted along low-energy facets, as observed experimentally with transmission electron microscope (TEM) imaging.[4,25,33,47,48,69] When two such faceted NPs are in close proximity, parallel alignment of facets at the gap can create a flat nanocavity, typically filled with a probe molecule or a dielectric spacer. Here, this geometry is modeled with a truncated nanosphere containing a circular facet of radius f at the cavity [Fig. 5(a)] surrounded by air; still, the two NPs are separated by 1 nm.

When the facet width $2f$ increases, a series of modifications on the plasmonic behaviors of the dimer hotspots are observed (Fig. 5). First, the BDP resonance gradually red shifts with increasing $2f$ from λ = 695 nm to 765 nm. The peak <EF> intensity first increases, reaching a maximum value of 1.1×10^9 at λ = 725 nm for f = 5 nm, and then suffers a 75 percent decrease. Meanwhile, the maximum EF monotonously decreases with increasing f, with values of 6.3×10^{10} and 1.0×10^{10} for f = 5 and 15 nm, respectively. The mapping of local field distributions [Fig. 6(a) and 6(b)] shows a large hotspot volume around the cavity, a transition sometimes referred to as hotspot to hot-zone.[70] The increase in hotspot volume at small f results in an increase in average near-field enhancement despite the decrease in maximum field enhancement.

In addition to the BDP mode, two distinct higher-order resonances are observed for highly faceted dimers. Surface charge distributions maps for f = 15 nm at λ = 640 and 520 nm [Fig. 6(g) and 6(h)] assist in identifying these resonances as bonding modes of l = 2 ("+ - + — - + -") and 3 ("+ - + - — + - + -"), respectively, with three and four poles, respectively, for each individual nanosphere. The near-field enhancement sustained by these higher order modes is relatively weak and the maximum EF is 1.6×10^9 and 9.8×10^6 [Fig. 6(c) and 6(d)].

Nanoroughness

Large polycrystalline metallic NPs with nanoscale roughened surfaces are of interest as they have demonstrated single-particle or enhanced SERS performance owing to strong intraparticle near-field coupling.[71-73] The radius of those particles varies from tens of nanometers to several microns, and their surfaces usually consist of many randomly arranged, irregular protrusions approximately 20-50 nm in size.[21,24,49-52] Here, we modeled such rough NPs using a set of 3D hierarchical structures with meatball-like morphology, as shown in Fig. 7. Each NP is treated as a core-shell structure with an inner Au nanosphere core and an outer nanoshell composed of a multitude of hemispherical Au protrusions.[73] The surface roughness is then tailored by the number, size and distribution of the hemispheres; here we fixed the number of hemispheres to 66, the underlying sphere radius to 50 nm, and used the hemisphere radius r to manipulate the roughness. Given these parameters, r = 12 nm is the critical value below which the hemispheres are separated from each other. As r decreases

from 30 to 12 nm, the roughness increases, causing the BDP mode to blue shift from λ = 695 to 650 nm. The peak <EF> intensity increases with roughness from 7.1×10^8 to 9.3×10^8 (Fig. 7).

Both the BDP and higher-order modes can be clearly identified in the plasmon mapping shown in Fig. 8, despite different surface roughness. The local field distributions of rough dimers resembles that of the idealized dimers of Fig. 2. However, the introduction of surface roughness increases the maximum EF compared to smooth NP dimers (7.9×10^{10}, λ = 695 nm; 5.0×10^9, λ = 570 nm); it reaches 1.3×10^{11} (r = 20 nm, λ = 655 nm), 8.5×10^9 (r = 20 nm, λ = 560 nm), 2.0×10^{11} (r = 12 nm, λ = 650 nm) and 9.5×10^9 (r = 12 nm, λ = 560 nm). This increase is attributed to the localization of conduction electrons at the substructural protrusions and the effect of nanogap curvature on the near-field enhancement.[74] However, the changes observed in maximum field enhancement due to surface roughness are small, because surface roughness mainly contributes to intraparticle near-field coupling, which remains weaker than the strong interparticle near-field coupling. For single NPs or dimers with wide gaps, the intraparticle near-field coupling is expected to play a larger role in the near-field enhancement.[73]

Far-field properties

In addition, we have calculated the far-field extinction cross sections for the bridged, creviced, faceted and roughened dimers, as illustrated in Fig. S1-S4. It is noted that there is a

one-to-one correspondence at nearly the same wavelengths between the near- and far-field resonance peaks.

While a distinct deviation of spectral positions between the near- and far-field plasmonic responses, especially for large particles, has been described,[73,75,76] the deviation here is minimal due to strong near-field coupling. This is of importance in practical applications because the presence of a far-field extinction peak indicates the wavelength of maximum near-field enhancement. It should also be noted that the extinction peak intensity is not positively related to the near-field enhancement intensity.

Conclusion

Beyond the ideal nanosphere dimer hotspot model, we have numerically demonstrated that small gap morphology variations may have great influences on the plasmonic properties of the NP hotspot systems. A series of NP dimer gap geometries are considered on the basis of published experiment reports, including nanobridge, nanocrevice, nanofacet and nanoroughness. For the dominant BDP mode, the introduction of conductive nanobridges results into a rapid degeneration of the hotspot, while the presence of sharp nanocrevices leads to large changes in both the resonance positions and intensities. The faceted NP dimers are likely to shift the resonance to the red region while the roughened ones gently shift the resonance to the blue region. Various hybridized plasmon modes including the CTP, BDP and higher-order modes were described and interestingly, all of them can be assigned to the

bonding LAP modes. This study of gap geometry effects on NP dimer hotspots provides a physical insight into the ongoing issues with the poor reproducibility of SERS substrates, and further gives rise to the need for the development of precision plasmonics.

Conflicts of interest

There are no conflicts of interest to declare.

Acknowledgements

The authors thank Prof. Wensheng Lai for the access to COMSOL Multiphysics software. This work was supported by the National Natural Science Foundation of China (51701068, 61775055) and the Fundamental Research Funds for the Central Universities (531107040995). E.R. acknowledges support from a 3M non-tenured faculty award and the Binational Science Foundation.

Notes and references

1 B. Sharma, R. R. Frontiera, A.-I. Henry, E. Ringe and R. P. Van Duyne, *Mater. Today*, 2012, **15**, 16-25.

2 S. Y. Ding, J. Yi, J. F. Li, B. Ren, D. Y. Wu, R. Panneerselvam and Z. Q. Tian, *Nat. Rev. Mater.*, 2016, **1**, 16021.

3 X. Wang, G. Ma, A. Li, J. Yu, Z. Yang, J. Lin, A. Li, X. Han and L. Guo, *Chem. Sci.*, 2018, **9**, 4009-4015.

4 K. L. Wustholz, A. I. Henry, J. M. McMahon, R. G. Freeman, N. Valley, M. E. Piotti, M. J. Natan, G. C. Schatz and R. P. Van Duyne, *J. Am. Chem. Soc.*, 2010, **132**, 10903-10910.

5 K. L. Kelly, E. Coronado, L. L. Zhao and G. C. Schatz, *J. Phys. Chem. B*, 2003, **107**, 668-677.

6 K.-i. Yoshida, T. Itoh, H. Tamaru, V. Biju, M. Ishikawa and Y. Ozaki, *Phys. Rev. B*, 2010, **81**, 115406.

7 T. Itoh, Y. S. Yamamoto and Y. Ozaki, *Chem. Soc. Rev.*, 2017, **46**, 3904-3921.

8 S. Nie and S. R. Emory, *Science*, 1997, **275**, 1102-1106.

9 K. Kneipp, Y. Wang, H. Kneipp, L. T. Perelman, I. Itzkan, R. Dasari and M. S. Feld, *Phys. Rev. Lett.*, 1997, **78**, 1667-1670.

10 S. L. Kleinman, E. Ringe, N. Valley, K. L. Wustholz, E. Phillips, K. A. Scheidt, G. C. Schatz and R. P. Van Duyne, *J. Am. Chem. Soc.*, 2011, **133**, 4115-4122.

11 W. Yan, L. Yang, J. Chen, Y. Wu, P. Wang and Z. Li, *Adv. Mater.*, 2017, **29**, 1702893.

12 T. Itoh, M. Iga, H. Tamaru, K.-i. Yoshida, V. Biju and M. Ishikawa, *J. Chem. Phys.*, 2012, **136**, 024703.

13 C. Huck, F. Neubrech, J. Vogt, A. Toma, D. Gerbert, J. Katzmann, T. Hartling and A. Pucci, *ACS Nano*, 2014, **8**, 4908-4914.

14 S. Kim, J. H. Jin, Y. J. Kim, I. Y. Park, Y. Kim and S. W. Kim, *Nature*, 2008, **453**, 757-760.

15 H. Aouani, M. Rahmani, M. Navarro-Cia and S. A. Maier, *Nat. Nanotechnol.*, 2014, **9**, 290-294.

16 M. Kauranen and A. V. Zayats, *Nat. Photonics*, 2012, **6**, 737-748.

17 H. Choo, M. K. Kim, M. Staffaroni, T. J. Seok, J. Bokor, S. Cabrini, P. J. Schuck, M. C. Wu and E. Yablonovitch, *Nat. Photonics*, 2012, **6**, 837-843.

18 J. Mertens, A. L. Eiden, D. O. Sigle, F. M. Huang, A. Lombardo, Z. P. Sun, R. S. Sundaram, A. Colli, C. Tserkezis, J. Aizpurua, S. Milana, A. C. Ferrari and J. J. Baumberg, *Nano Lett.*, 2013, **13**, 5033-5038.

19 M. S. Tame, K. R. McEnery, S. K. Oezdemir, J. Lee, S. A. Maier and M. S. Kim, *Nat. Phys.*, 2013, **9**, 329-340.

20 S. F. Tan, L. Wu, J. K. W. Yang, P. Bai, M. Bosman and C. A. Nijhuis, *Science*, 2014, **343**, 1496-1499.

21 S. Gwo, H. Y. Chen, M. H. Lin, L. Y. Sun and X. Q. Li, *Chem. Soc. Rev.*, 2016, **45**, 5672-5716.

22 H. Wei and H. Xu, *Nanoscale*, 2013, **5**, 10794-10805.

23 Y. Huang, Q. Zhou, M. Hou, L. Ma and Z. Zhang, *Phys. Chem. Chem. Phys.*, 2015, **17**, 29293-29298.

24 J. H. Yoon, F. Selbach, L. Langolf and S. Schlucker, *Small*, 2018, **14**, 1702754.

25 P. S. Popp, J. F. Herrmann, E. C. Fritz, B. J. Ravoo and C. Hoppener, *Small*, 2016, **12**, 1667-1675.

26 Y. Huang, Y. Chen, X. Xue, Y. Zhai, L. Wang and Z. Zhang, *Opt. Lett.*, 2018, **43**, 2332-2335.

27 E. Prodan, C. Radloff, N. J. Halas and P. Nordlander, *Science*, 2003, **302**, 419-422.

28 F. Q. Huang, G. S. Ma, J. Z. Liu, J. Lin, X. Wang and L. Guo, *Small*, 2016, **12**, 5442-5448.

29 E. Ringe, J. M. McMahon, K. Sohn, C. Cobley, Y. N. Xia, J. X. Huang, G. C. Schatz, L. D. Marks and R. P. Van Duyne, *J. Phys. Chem. C*, 2010, **114**, 12511-12516.

30 J. A. McMahon, Y. M. Wang, L. J. Sherry, R. P. Van Duyne, L. D. Marks, S. K. Gray and G. C. Schatz, *J. Phys. Chem. C*, 2009, **113**, 2731-2735.

31 R. Esteban, G. Aguirregabiria, A. G. Borisov, Y. M. M. Wang, P. Nordlander, G. W. Bryant and J. Aizpurua, *ACS Photonics*, 2015, **2**, 295-305.

32 C. Tserkezis, R. Esteban, D. O. Sigle, J. Mertens, L. O. Herrmann, J. J. Baumberg and J. Aizpurua, *Phys. Rev. A*, 2015, **92**, 053811.

33 J. H. Huh, J. Lee and S. Lee, *ACS Photonics*, 2018, **5**, 413-421.

34 E. Ringe, M. R. Langille, K. Sohn, J. Zhang, J. X. Huang, C. A. Mirkin, R. P. Van Duyne and L. D. Marks, *J. Phys. Chem. Lett.*, 2012, **3**, 1479-1483.

35 M. N. O'Brien, M. R. Jones, K. A. Brown and C. A. Mirkin, *J. Am. Chem. Soc.*, 2014, **136**, 7603-7606.

36 A. Kuhlicke, S. Schietinger, C. Matyssek, K. Busch and O. Benson, *Nano Lett.*, 2013, **13**, 2041-2046.

37 J. T. Hugall, J. J. Baumberg and S. Mahajan, *J. Phys. Chem. C*, 2012, **116**, 6184-6190.

38 D. O. Sigle, J. Mertens, L. O. Herrmann, R. W. Bowman, S. Ithurria, B. Dubertret, Y. M. Shi, H. Y. Yang, C. Tserkezis, J. Aizpurua and J. J. Baumberg, *ACS Nano*, 2015, **9**, 825-830.

39 A. Teulle, M. Bosman, C. Girard, K. L. Gurunatha, M. Li, S. Mann and E. Dujardin, *Nat. Mater.*, 2015, **14**, 87-94.

40 A. N. Koya and J. Q. Lin, *Appl. Phys. Rev.*, 2017, **4**, 021104.

41 A. N. Koya and J. Q. Lin, *J. Appl. Phys.*, 2016, **120**, 093105.

42 F. F. Wen, Y. Zhang, S. Gottheim, N. S. King, Y. Zhang, P. Nordlander and N. J. Halas, *ACS Nano*, 2015, **9**, 6428-6435.

43 H. G. Duan, A. I. Fernandez-Dominguez, M. Bosman, S. A. Maier and J. K. W. Yang, *Nano Lett.*, 2012, **12**, 1683-1689.

44 F. J. GarciaVidal and J. B. Pendry, *Phys. Rev. Lett.*, 1996, **77**, 1163-1166.

45 H. X. Xu, J. Aizpurua, M. Kall and P. Apell, *Phys. Rev. E*, 2000, **62**, 4318-4324.

46 J. M. Nam, J. W. Oh, H. Lee and Y. D. Suh, *Acc. Chem. Res.*, 2016, **49**, 2746-2755.

47 S. Marhaba, G. Bachelier, C. Bonnet, M. Broyer, E. Cottancin, N. Grillet, J. Lerme, J. L. Vialle and M. Pellarin, *J. Phys. Chem. C*, 2009, **113**, 4349-4356.

48 M.-E. Kleemann, J. Mertens, X. Zheng, S. Cormier, V. Turek, F. Benz, R. Chikkaraddy, W. Deacon, A. Lombardi, V. V. Moshchalkov, G. A. E. Vandenbosch and J. J. Baumberg, *ACS Nano*, 2017, **11**, 850-855.

49 H. Wang, G. P. Goodrich, F. Tam, C. Oubre, P. Nordlander and N. J. Halas, *J. Phys. Chem. B*, 2005, **109**, 11083-11087.

50 H. Wang and N. J. Halas, *Adv. Mater.*, 2008, **20**, 820-825.

51 H. X. Lin, J. M. Li, B. J. Liu, D. Y. Liu, J. X. Liu, A. Terfort, Z. X. Xie, Z. Q. Tian and B. Ren, *Phys. Chem. Chem. Phys.*, 2013, **15**, 4130-4135.

52 H. B. Tang, G. W. Meng, Z. B. Li, C. H. Zhu, Z. L. Huang, Z. M. Wang and F. D. Li, *Nano Res.*, 2015, **8**, 2261-2270.

53 Y. J. Lee, N. B. Schade, L. Sun, J. A. Fan, D. R. Bae, M. M. Mariscal, G. Lee, F. Capasso, S. Sacanna, V. N. Manoharan and G. R. Yi, *ACS Nano*, 2013, **7**, 11064-11070.

54 H. Kollmann, X. Piao, M. Esmann, S. F. Becker, D. C. Hou, C. Huynh, L. O. Kautschor, G. Bosker, H. Vieker, A. Beyer, A. Golzhauser, N. Park, R. Vogelgesang, M. Silies and C. Lienau, *Nano Lett.*, 2014, **14**, 4778-4784.

55 R. Esteban, A. G. Borisov, P. Nordlander and J. Aizpurua, *Nat. Commun.*, 2012, **3**, 825.

56 W. Q. Zhu and K. B. Crozier, *Nat. Commun.*, 2014, **5**, 5228.

57 E. D. Palik, *Handbook of Optical Constants of Solid*, Academic Press, New York, 1985.

58 A. D. Rakic, A. B. Djurisic, J. M. Elazar and M. L. Majewski, *Appl. Opt.*, 1998, **37**, 5271-5283.

59 Y. Huang, L. Ma, J. Li and Z. Zhang, *Nanotechnology*, 2017, **28**, 105203.

60 T. Itoh, Y. S. Yamamoto, H. Tamaru, V. Biju, S.-i. Wakida and Y. Ozaki, *Phys. Rev. B*, 2014, **89**, 195436.

61 Y. Huang, X. Zhang, E. Ringe, M. Hou, L. Ma and Z. Zhang, *Sci. Rep.*, 2016, **6**, 23159.

62 Y. Huang, X. Zhang, E. Ringe, L. Ma, X. Zhai, L. Wang and Z. Zhang, *Nanoscale*, 2018, **10**, 4267-4275.

63 Y. Huang, X. Zhang, J. H. Li, L. W. Ma and Z. J. Zhang, *J. Mater. Chem. C*, 2017, **5**, 6079-6085.

64 E. Kazuma and T. Tatsuma, *J. Phys. Chem. C*, 2013, **117**, 2435-2441.

65 L. Bachenheimer, P. Elliott, S. Stagon and H. Huang, *Appl. Phys. Lett.*, 2014, **105**, 213104.

66 L. Ma, Y. Huang, M. Hou, J. Li, Z. Xie and Z. Zhang, *J. Phys. Chem. C*, 2016, **120**, 606-615.

67 Y. Huang, L. Ma, M. Hou, Z. Xie and Z. Zhang, *Phys. Chem. Chem. Phys.*, 2016, **18**, 2319-2323.

68 L. F. Liu, Y. M. Wang, Z. Y. Fang and K. Zhao, *J. Chem. Phys.*, 2013, **139**, 064310.

69 E. Ringe, R. P. Van Duyne and L. D. Marks, *J. Phys. Chem. C*, 2013, **117**, 15859-15870.

70 J. P. Litz, J. P. Camden and D. J. Masiello, *J. Phys. Chem. Lett.*, 2011, **2**, 1695-1700.

71 Q. F. Zhang, N. Large and H. Wang, *ACS Appl. Mater. Inter.*, 2014, **6**, 17255-17267.

72 Z. Liu, F. L. Zhang, Z. B. Yang, H. J. You, C. F. Tian, Z. Y. Li and J. X. Fang, *J. Mater. Chem. C*, 2013, **1**, 5567-5576.

73 Y. Huang, Y. Chen, W. Gao, Z. Yang and L. Wang, *Appl. Phys. Lett.*, 2018, **112**, 171906.

74 D. Lee and S. Yoon, *J. Phys. Chem. C*, 2016, **120**, 20642-20650.

75 J. Zuloaga and P. Nordlander, *Nano Lett.*, 2011, **11**, 1280-1283.

76 M. D. Doherty, A. Murphy, R. J. Pollard and P. Dawson, *Phys. Rev. X*, 2013, **3**, 011001.

Figures

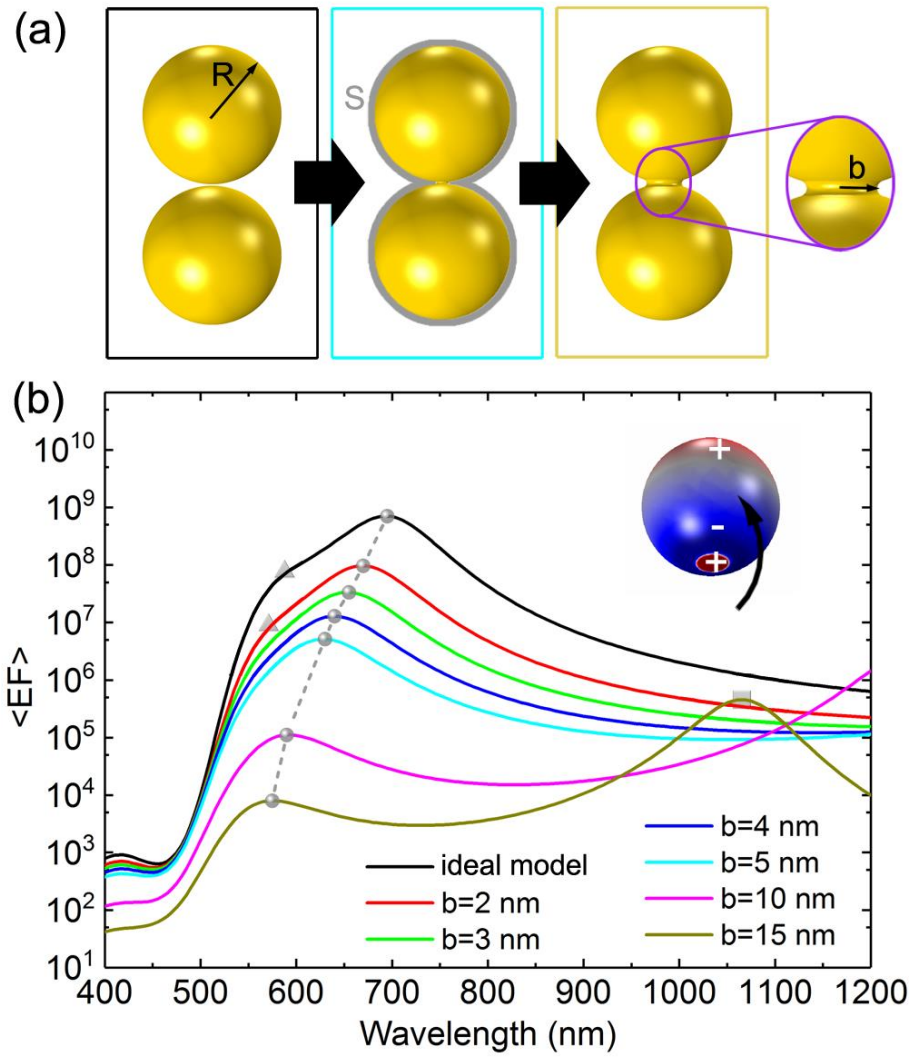

Fig. 1 (a) Morphology evolution of bridged Au NP dimers with R = 50 nm. The radius of the thin Au cylindrical bridge is b. From left to right, the model corresponds to the idealized nanosphere dimer and the bridged dimers with b = 5, 15 nm respectively. As an example, the area for <EF> calculation is schematically indicated by the grey outlines S. (b) FEM calculated wavelength-dependent near-field <EF> spectra for the bridge dimers. The CTP, BDP and bonding l =2 modes are marked by square, circle and triangle symbols respectively.

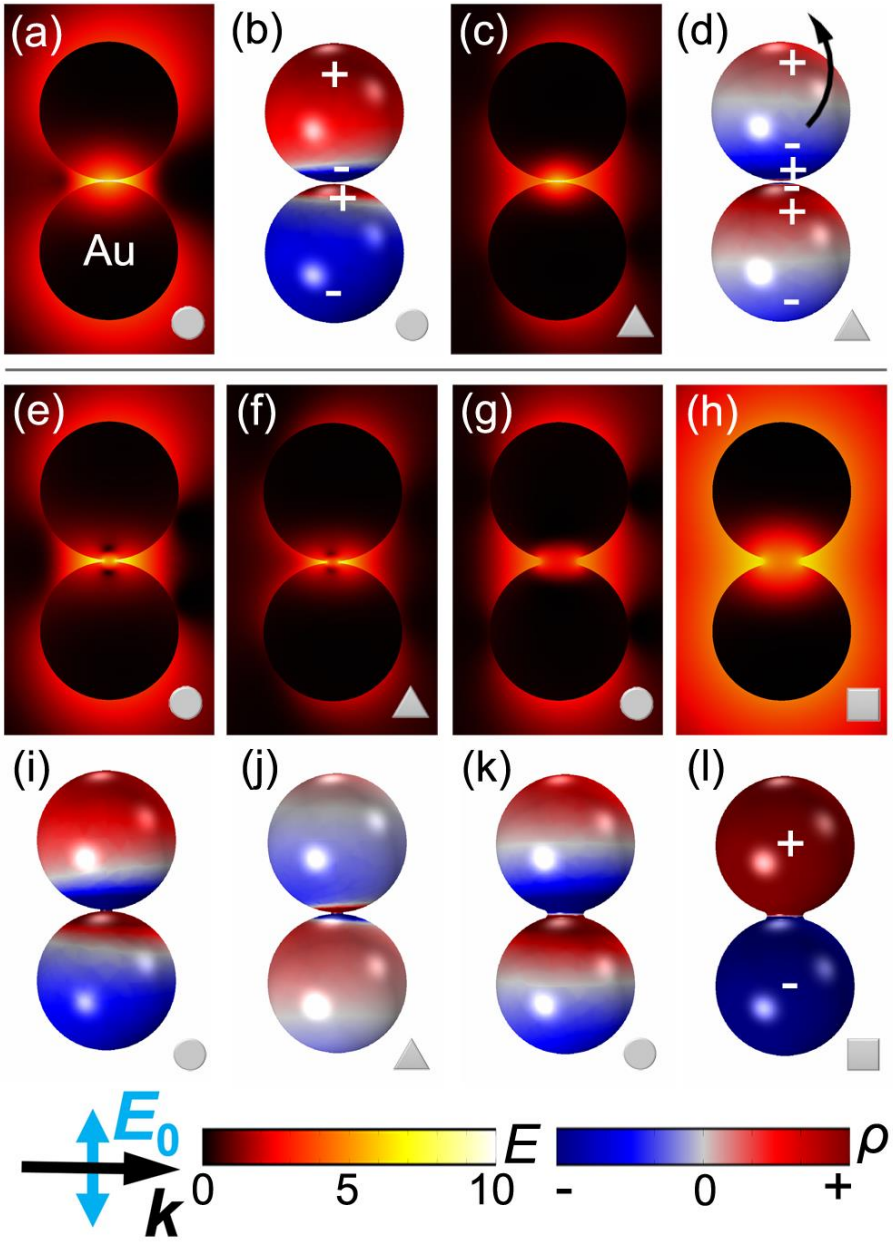

Fig. 2 FEM plasmon mapping. (a) Local electric field distributions in the form of logarithmic EF ($\lg(|\boldsymbol{E}|^4/|\boldsymbol{E}_0|^4)$) at λ = 695 nm for the idealized dimer, and (b) corresponding 3D surface charge distributions. Red color represents positive charge while blue is negative. The mapping reveals the BDP mode. (c)-(d) Similarly, the electric field and surface charge distributions at λ = 570 nm for the idealized dimer. Note that an oblique view for the surface charge poles is inserted in Fig. 1(b), demonstrating the higher-order bonding mode l = 2. (e)-

(h) Electric field distributions for bridged dimers with (e) b = 5 nm, λ = 630 nm; (f) b = 5 nm, λ = 550 nm; (g) b = 15 nm, λ = 575 nm; (h) b = 15 nm, λ = 1065 nm. (i)-(l) Corresponding surface charge distributions. In particular, the mapping (l) reveals the CTP mode. $\boldsymbol{k}$ is the wave vector and $\boldsymbol{E_0}$ is the incident polarization.

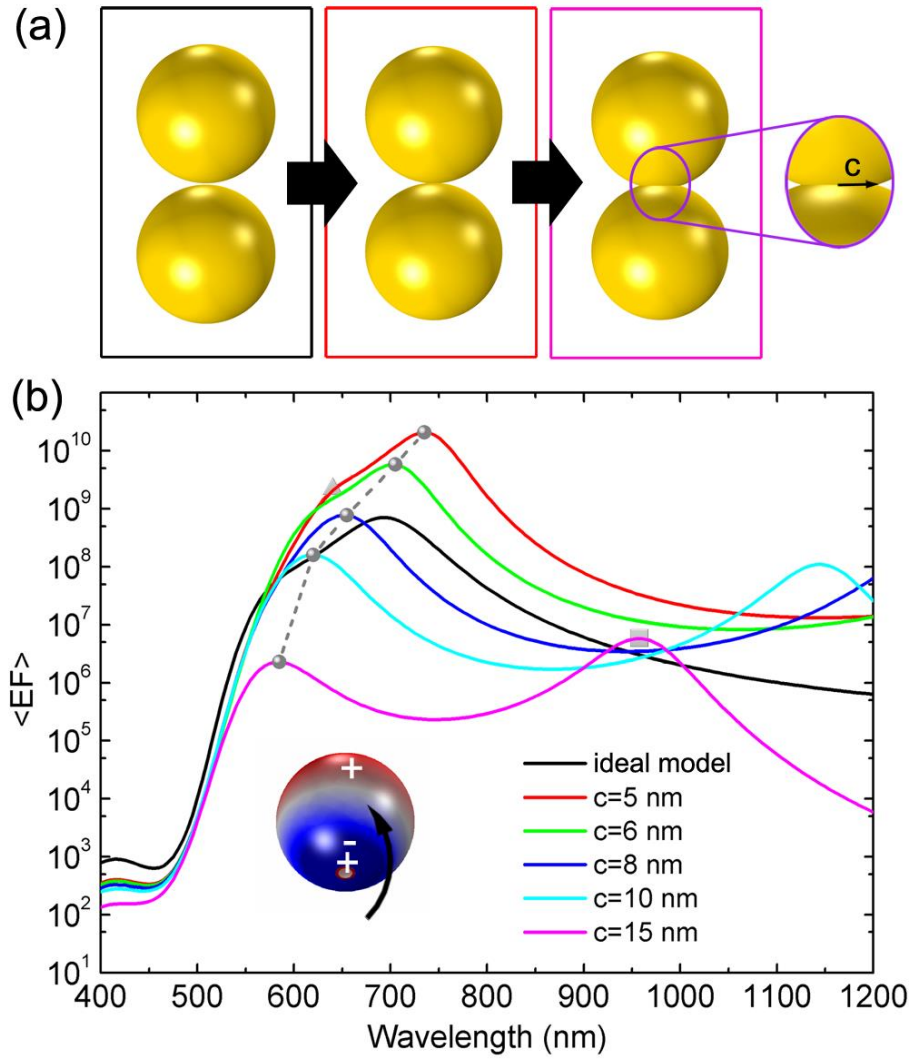

Fig. 3 (a) Creviced dimers with R = 50 nm, where the crevice size is determined the intersecting facet radius c. From left to right, the model corresponds to the idealized dimer and the creviced ones c = 5, 15 nm respectively. (b) Calculated <EF> spectra of the creviced dimers.

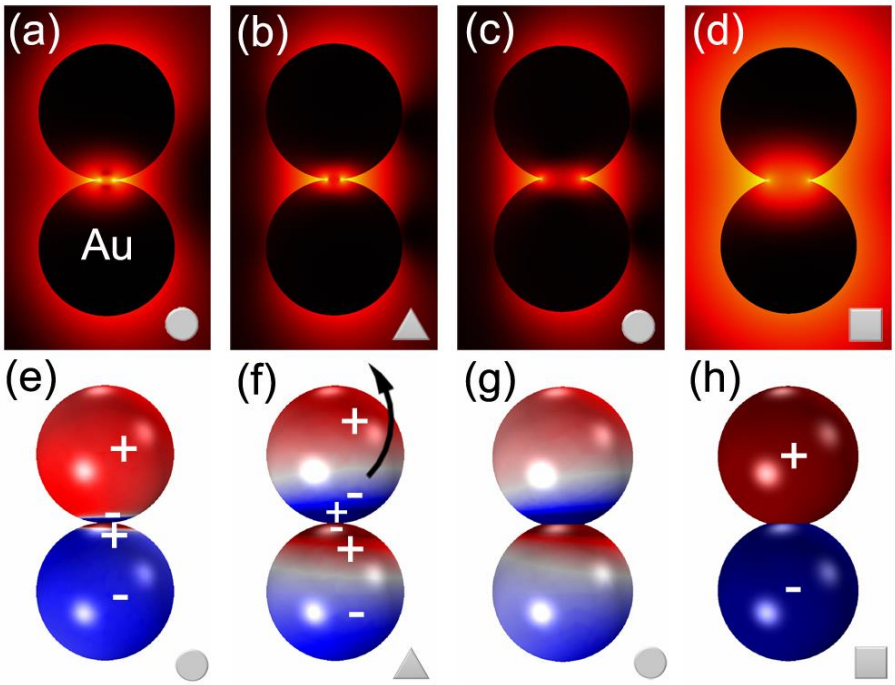

Fig. 4 (a)-(d) Typical electric field distributions for the creviced dimers: (a) c = 5 nm, λ = 735 nm; (b) c = 5 nm, λ = 640 nm; (c) c = 15 nm, λ = 585 nm; (d) c = 15 nm, λ = 955 nm. (e)-(h) Corresponding surface charge distributions. Note that an oblique view for the surface charge poles of the upper NP in (f) is inserted in Fig. 3(b). The mapping method and color tables are the same as those in Fig. 2.

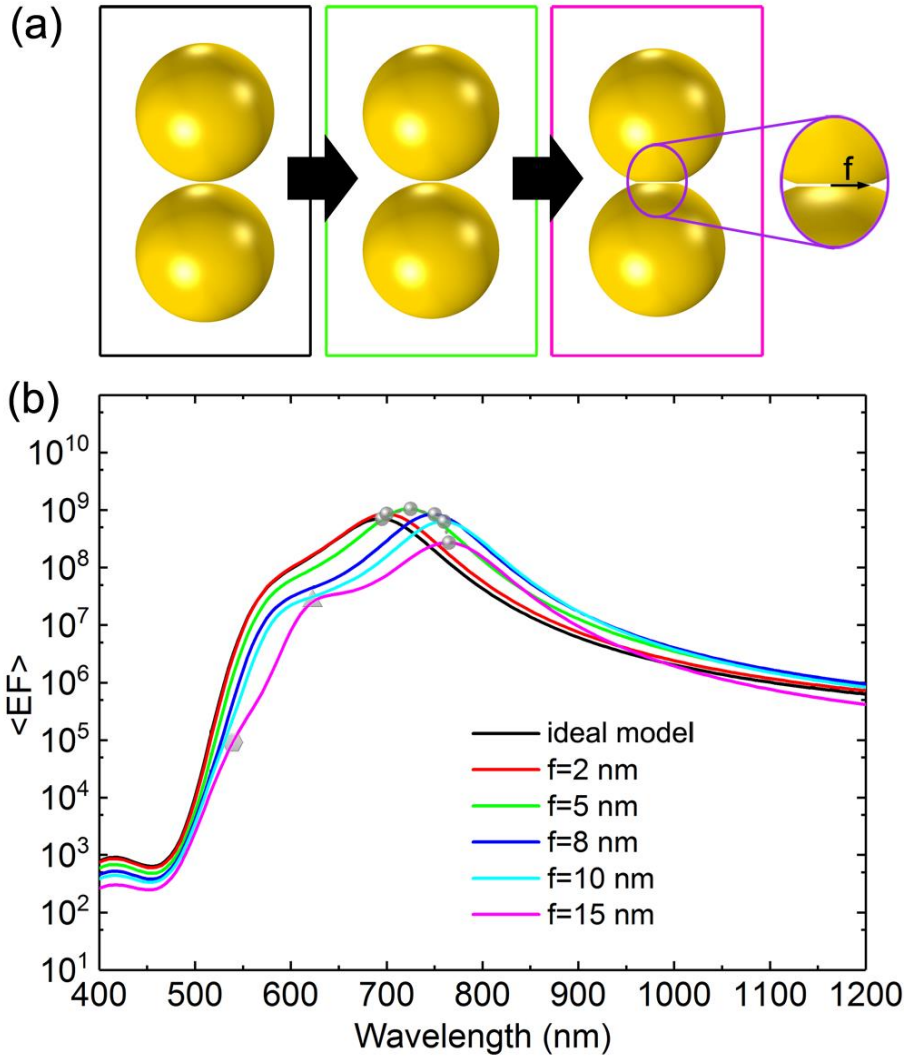

Fig. 5 (a) Models of the faceted dimers with R = 50 nm. f is the radius of the circular facet at the gap. The model corresponds to the idealized dimer and faceted dimers with f = 5, 15 nm respectively. (b) Calculated <EF> spectra as f is increased from 2 to 15 nm.

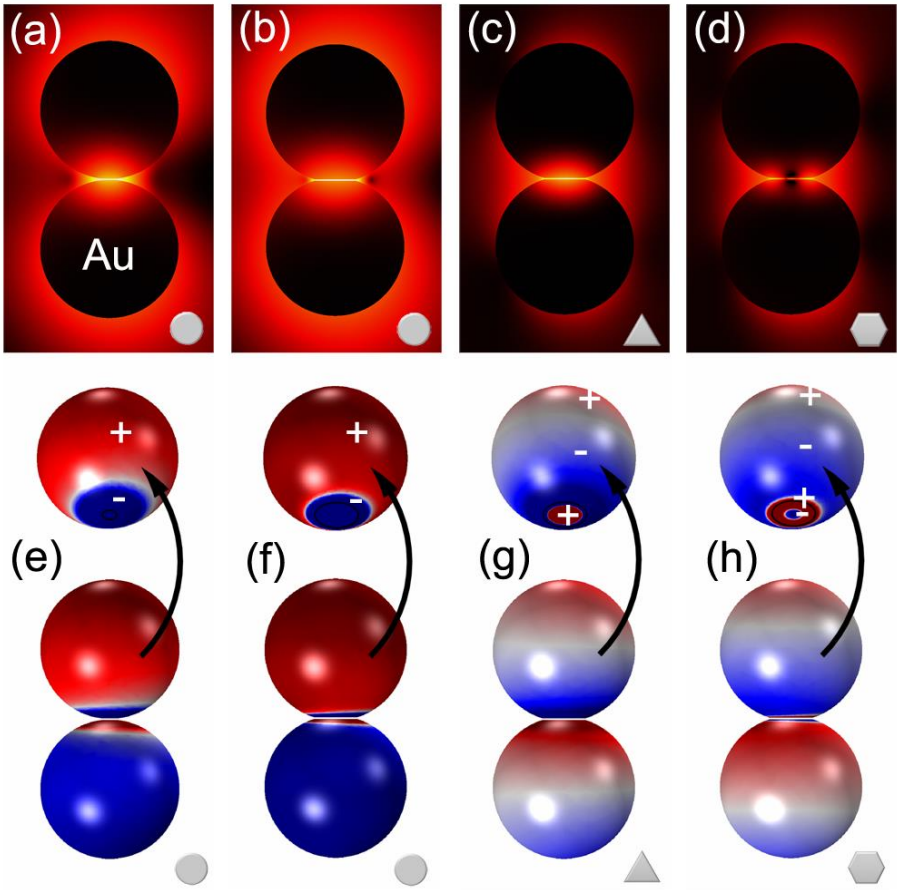

Fig. 6 (a)-(d) Typical electric field distributions for the faceted dimers: (a) f = 5 nm, λ = 725 nm; (b) f = 15 nm, λ = 765 nm; (c) f = 15 nm, λ = 620 nm; (d) f = 15 nm, λ = 540 nm. (e)-(h) Corresponding surface charge distributions. For each mapping, an oblique view for the surface charge poles of the upper NP is presented. The black circle at the bottom of the oblique NP indicates the position and size of the facet. The mapping method and color tables are the same as those in Fig. 2.

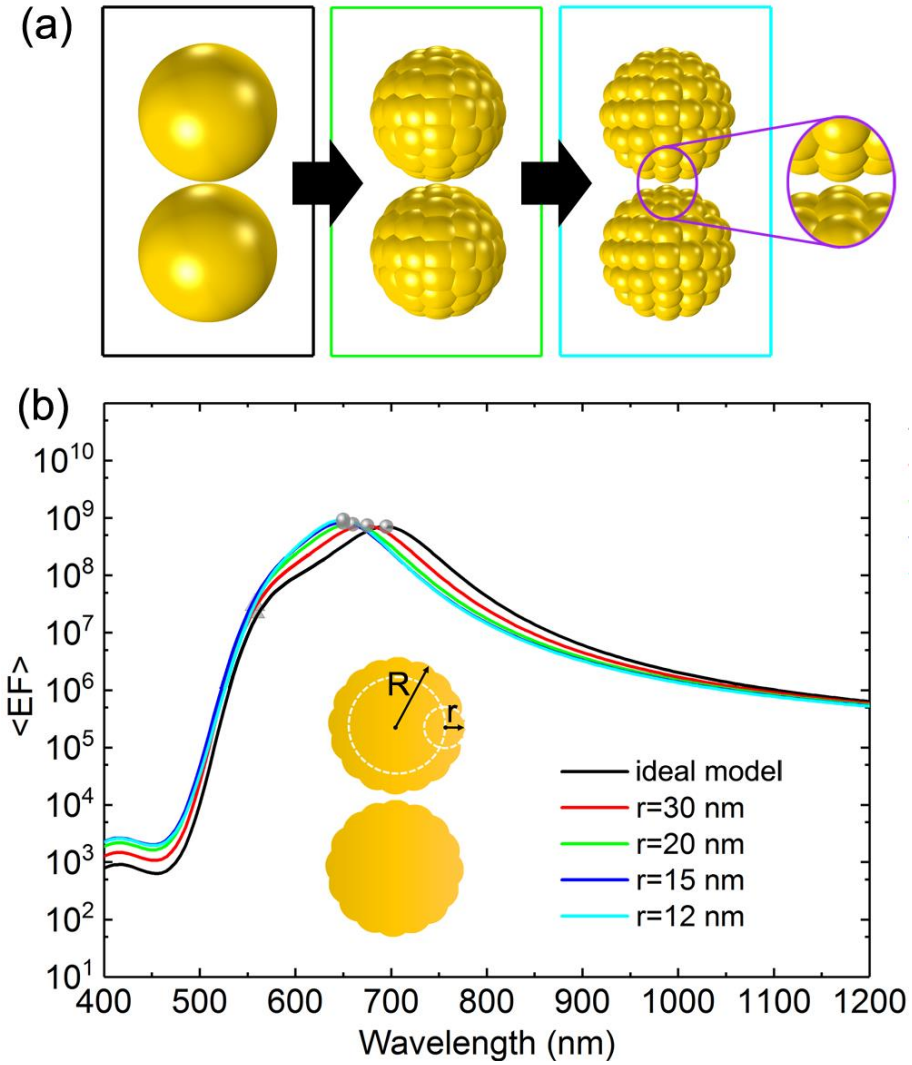

Fig. 7 Near-field enhancement from roughened dimers with R = 50 nm. (a) Morphology evolution of the roughened dimers. The surface roughness is tailored by the radius r of the hemispherical protrusions. From left to right, the model corresponds to the idealized dimer and roughened dimers with r = 20, 12 nm. (b) Calculated wavelength-dependent <EF> spectra of the roughened dimers. The inset shows a cross section of the dimer structure in the symmetry plane.

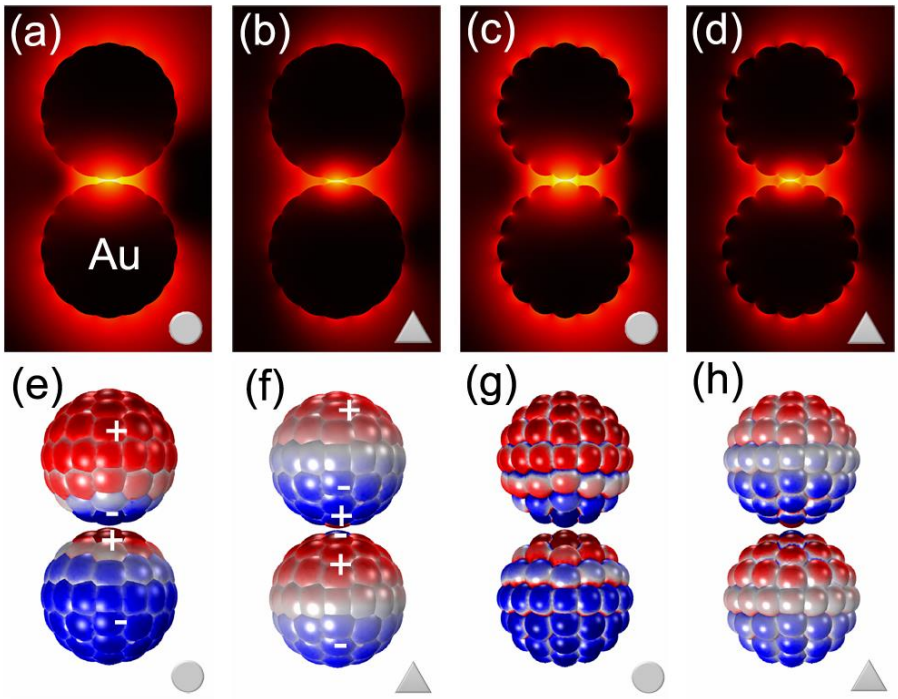

Fig. 8 (a)-(d) Electric field distributions of roughened dimers: (a) r = 20 nm, λ = 655 nm; (b) r = 20 nm, λ = 560 nm; (c) r = 12 nm, λ = 650 nm; (d) r = 12 nm, λ = 560 nm. (e)-(h) Corresponding surface charge distributions. The mapping method and color tables are the same as those in Fig. 2.